

$\Upsilon(1S+2S+3S)$ production in $d+Au$ and $p+p$ collisions at $\sqrt{s_{NN}}=200$ GeV and cold-nuclear-matter effects

A. Adare,¹² S. Afanasiev,²⁹ C. Aidala,^{37,41} N.N. Ajitanand,⁵⁹ Y. Akiba,^{53,54} R. Akimoto,¹¹ H. Al-Bataineh,⁴⁷ H. Al-Ta'ani,⁴⁷ J. Alexander,⁵⁹ K.R. Andrews,¹ A. Angerami,¹³ K. Aoki,^{34,53} N. Apadula,⁶⁰ L. Aphecetche,⁶¹ E. Appelt,⁶⁵ Y. Aramaki,^{11,53} R. Armendariz,⁷ J. Asai,⁵³ E.C. Aschenauer,⁶ E.T. Atomssa,³⁵ R. Averbeck,⁶⁰ T.C. Awes,⁴⁹ B. Azmoun,⁶ V. Babintsev,²⁴ M. Bai,⁵ G. Baksay,¹⁹ L. Baksay,¹⁹ A. Baldisseri,¹⁵ B. Bannier,⁶⁰ K.N. Barish,⁷ P.D. Barnes,^{37,*} B. Bassalleck,⁴⁶ A.T. Basye,¹ S. Bathe,^{7,54} S. Batsouli,⁴⁹ V. Baublis,⁵² C. Baumann,⁴² A. Bazilevsky,⁶ S. Belikov,^{6,*} R. Belmont,⁶⁵ J. Ben-Benjamin,⁴³ R. Bennett,⁶⁰ A. Berdnikov,⁵⁶ Y. Berdnikov,⁵⁶ J.H. Bhom,⁶⁹ A.A. Bickley,¹² D.S. Blau,³³ J.G. Boissevain,³⁷ J.S. Bok,⁶⁹ H. Borel,¹⁵ K. Boyle,^{54,60} M.L. Brooks,³⁷ D. Broxmeyer,⁴³ H. Buesching,⁶ V. Bumazhnov,²⁴ G. Bunce,^{6,54} S. Butsyk,³⁷ C.M. Camacho,³⁷ S. Campbell,⁶⁰ A. Caringi,⁴³ P. Castera,⁶⁰ B.S. Chang,⁶⁹ W.C. Chang,² J.-L. Charvet,¹⁵ C.-H. Chen,⁶⁰ S. Chernichenko,²⁴ C.Y. Chi,¹³ M. Chiu,^{6,25} I.J. Choi,^{25,69} J.B. Choi,⁹ R.K. Choudhury,⁴ P. Christiansen,³⁹ T. Chujo,⁶⁴ P. Chung,⁵⁹ A. Churnin,²⁴ O. Chvala,⁷ V. Cianciolo,⁴⁹ Z. Citron,⁶⁰ B.A. Cole,¹³ Z. Conesa del Valle,³⁵ M. Connors,⁶⁰ P. Constantin,³⁷ M. Csanád,¹⁷ T. Csörgő,⁶⁸ T. Dahms,⁶⁰ S. Dairaku,^{34,53} I. Danchev,⁶⁵ K. Das,²⁰ A. Datta,⁴¹ G. David,⁶ M.K. Dayananda,²¹ A. Denisov,²⁴ D. d'Enterria,³⁵ A. Deshpande,^{54,60} E.J. Desmond,⁶ K.V. Dharmawardane,⁴⁷ O. Dietzsch,⁵⁷ A. Dion,^{28,60} M. Donadelli,⁵⁷ O. Drapier,³⁵ A. Drees,⁶⁰ K.A. Drees,⁵ A.K. Dubey,⁶⁷ J.M. Durham,⁶⁰ A. Durum,²⁴ D. Dutta,⁴ V. Dzhordzhadze,⁷ L. D'Orazio,⁴⁰ S. Edwards,²⁰ Y.V. Efremenko,⁴⁹ F. Ellinghaus,¹² T. Engelmores,¹³ A. Enokizono,^{36,49} H. En'yo,^{53,54} S. Esumi,⁶⁴ K.O. Eysler,⁷ B. Fadem,⁴³ D.E. Fields,^{46,54} M. Finger,⁸ M. Finger, Jr.,⁸ F. Fleuret,³⁵ S.L. Fokin,³³ Z. Fraenkel,^{67,*} J.E. Frantz,^{48,60} A. Franz,⁶ A.D. Frawley,²⁰ K. Fujiwara,⁵³ Y. Fukao,^{34,53} T. Fusayasu,⁴⁵ I. Garishvili,⁶² A. Glenn,^{12,36} H. Gong,⁶⁰ X. Gong,⁵⁹ M. Gonin,³⁵ J. Gosset,¹⁵ Y. Goto,^{53,54} R. Granier de Cassagnac,³⁵ N. Grau,¹³ S.V. Greene,⁶⁵ G. Grim,³⁷ M. Grosse Perdekamp,^{25,54} T. Gunji,¹¹ L. Guo,³⁷ H.-Å. Gustafsson,^{39,*} A. Hadj Henni,⁶¹ J.S. Haggerty,⁶ K.I. Hahn,¹⁸ H. Hamagaki,¹¹ J. Hamblen,⁶² R. Han,⁵¹ J. Hanks,¹³ C. Harper,⁴³ E.P. Hartouni,³⁶ K. Haruna,²³ K. Hashimoto,^{53,55} E. Haslum,³⁹ R. Hayano,¹¹ X. He,²¹ M. Heffner,³⁶ T.K. Hemmick,⁶⁰ T. Hester,⁷ J.C. Hill,²⁸ M. Hohlmann,¹⁹ R.S. Hollis,⁷ W. Holzmann,^{13,59} K. Homma,²³ B. Hong,³² T. Horaguchi,^{11,23,53,64} Y. Hori,¹¹ D. Hornback,^{49,62} S. Huang,⁶⁵ T. Ichihara,^{53,54} R. Ichimiya,⁵³ H. Iinuma,^{31,34,53} Y. Ikeda,^{53,55,64} K. Imai,^{34,53} J. Imrek,¹⁶ M. Inaba,⁶⁴ A. Iordanova,⁷ D. Isenhower,¹ M. Ishihara,⁵³ T. Isobe,^{11,53} M. Issah,^{59,65} A. Isupov,²⁹ D. Ivanischev,⁵² Y. Iwanaga,²³ B.V. Jacak,^{60,†} J. Jia,^{6,13,59} X. Jiang,³⁷ J. Jin,¹³ D. John,⁶² B.M. Johnson,⁶ T. Jones,¹ K.S. Joo,⁴⁴ D. Jouan,⁵⁰ D.S. Jumper,¹ F. Kajihara,¹¹ S. Kametani,⁵³ N. Kamihara,⁵⁴ J. Kamin,⁶⁰ S. Kaneti,⁶⁰ B.H. Kang,²² J.H. Kang,⁶⁹ J.S. Kang,²² J. Kapustinsky,³⁷ K. Karatsu,^{34,53} M. Kasai,^{53,55} D. Kawall,^{41,54} M. Kawashima,^{53,55} A.V. Kazantsev,³³ T. Kempel,²⁸ A. Khanzadeev,⁵² K.M. Kijima,²³ J. Kikuchi,⁶⁶ A. Kim,¹⁸ B.I. Kim,³² D.H. Kim,⁴⁴ D.J. Kim,^{30,69} E. Kim,⁵⁸ E.-J. Kim,⁹ S.H. Kim,⁶⁹ Y.-J. Kim,²⁵ Y.K. Kim,²² E. Kinney,¹² K. Kiriluk,¹² Á. Kiss,¹⁷ E. Kistenev,⁶ J. Klay,³⁶ C. Klein-Boesing,⁴² D. Kleinjan,⁷ P. Kline,⁶⁰ L. Kochenda,⁵² B. Komkov,⁵² M. Konno,⁶⁴ J. Koster,²⁵ D. Kotov,⁵² A. Kozlov,⁶⁷ A. Král,¹⁴ A. Kravitz,¹³ G.J. Kunde,³⁷ K. Kurita,^{53,55} M. Kurosawa,⁵³ M.J. Kweon,³² Y. Kwon,^{62,69} G.S. Kyle,⁴⁷ R. Lacey,⁵⁹ Y.S. Lai,¹³ J.G. Lajoie,²⁸ D. Layton,²⁵ A. Lebedev,²⁸ D.M. Lee,³⁷ J. Lee,¹⁸ K.B. Lee,³² K.S. Lee,³² S.H. Lee,⁶⁰ S.R. Lee,⁹ T. Lee,⁵⁸ M.J. Leitch,³⁷ M.A.L. Leite,⁵⁷ B. Lenzi,⁵⁷ X. Li,¹⁰ P. Lichtenwalner,⁴³ P. Liebing,⁵⁴ S.H. Lim,⁶⁹ L.A. Linden Levy,¹² T. Liška,¹⁴ A. Litvinenko,²⁹ H. Liu,^{37,47} M.X. Liu,³⁷ B. Love,⁶⁵ D. Lynch,⁶ C.F. Maguire,⁶⁵ Y.I. Makdisi,⁵ A. Malakhov,²⁹ M.D. Malik,⁴⁶ A. Manion,⁶⁰ V.I. Manko,³³ E. Mannel,¹³ Y. Mao,^{51,53} L. Mašek,^{8,27} H. Masui,⁶⁴ F. Matathias,¹³ M. McCumber,⁶⁰ P.L. McGaughey,³⁷ D. McGlinchey,²⁰ C. McKinney,²⁵ N. Means,⁶⁰ M. Mendoza,⁷ B. Meredith,²⁵ Y. Miake,⁶⁴ T. Mibe,³¹ A.C. Mignerey,⁴⁰ P. Mikeš,²⁷ K. Miki,^{53,64} A. Milov,^{6,67} M. Mishra,³ J.T. Mitchell,⁶ Y. Miyachi,^{53,63} A.K. Mohanty,⁴ H.J. Moon,⁴⁴ Y. Morino,¹¹ A. Morreale,⁷ D.P. Morrison,⁶ S. Motschwiller,⁴³ T.V. Moukhanova,³³ D. Mukhopadhyay,⁶⁵ T. Murakami,³⁴ J. Murata,^{53,55} S. Nagamiya,³¹ J.L. Nagle,¹² M. Naglis,⁶⁷ M.I. Nagy,^{17,68} I. Nakagawa,^{53,54} Y. Nakamiya,²³ K.R. Nakamura,^{34,53} T. Nakamura,^{23,53} K. Nakano,^{53,63} S. Nam,¹⁸ J. Newby,³⁶ M. Nguyen,⁶⁰ M. Nihashi,²³ T. Niita,⁶⁴ R. Nouicer,⁶ A.S. Nyanin,³³ C. Oakley,²¹ E. O'Brien,⁶ S.X. Oda,¹¹ C.A. Ogilvie,²⁸ M. Oka,⁶⁴ K. Okada,⁵⁴ Y. Onuki,⁵³ A. Oskarsson,³⁹ M. Ouchida,^{23,53} K. Ozawa,¹¹ R. Pak,⁶ A.P.T. Palounek,³⁷ V. Pantuev,^{26,60} V. Papavassiliou,⁴⁷ B.H. Park,²² I.H. Park,¹⁸ J. Park,⁵⁸ S.K. Park,³² W.J. Park,³² S.F. Pate,⁴⁷ H. Pei,²⁸ J.-C. Peng,²⁵ H. Pereira,¹⁵ V. Peresedov,²⁹ D.Yu. Peressounko,³³ R. Petti,⁶⁰ C. Pinkenburg,⁶ R.P. Pisani,⁶ M. Proissl,⁶⁰ M.L. Purschke,⁶ A.K. Purwar,³⁷ H. Qu,²¹ J. Rak,^{30,46} A. Rakotozafindrabe,³⁵ I. Ravinovich,⁶⁷ K.F. Read,^{49,62} S. Rembeczki,¹⁹ K. Reygers,⁴² V. Riabov,⁵² Y. Riabov,⁵² E. Richardson,⁴⁰ D. Roach,⁶⁵ G. Roche,³⁸ S.D. Rolnick,⁷ M. Rosati,²⁸ C.A. Rosen,¹² S.S.E. Rosendahl,³⁹ P. Rosnet,³⁸ P. Rukoyatkin,²⁹ P. Ružička,²⁷ V.L. Rykov,⁵³ B. Sahlmueller,^{42,60}

N. Saito,^{31,34,53,54} T. Sakaguchi,⁶ S. Sakai,⁶⁴ K. Sakashita,^{53,63} V. Samsonov,⁵² S. Sano,^{11,66} M. Sarsour,²¹ T. Sato,⁶⁴ M. Savastio,⁶⁰ S. Sawada,³¹ K. Sedgwick,⁷ J. Seele,¹² R. Seidl,^{25,54} A.Yu. Semenov,²⁸ V. Semenov,²⁴ R. Seto,⁷ D. Sharma,⁶⁷ I. Shein,²⁴ T.-A. Shibata,^{53,63} K. Shigaki,²³ H.H. Shim,³² M. Shimomura,⁶⁴ K. Shoji,^{34,53} P. Shukla,⁴ A. Sickles,⁶ C.L. Silva,^{28,57} D. Silvermyr,⁴⁹ C. Silvestre,¹⁵ K.S. Sim,³² B.K. Singh,³ C.P. Singh,³ V. Singh,³ M. Slunečka,⁸ T. Sodre,⁴³ A. Soldatov,²⁴ R.A. Soltz,³⁶ W.E. Sondheim,³⁷ S.P. Sorensen,⁶² I.V. Sourikova,⁶ F. Staley,¹⁵ P.W. Stankus,⁴⁹ E. Stenlund,³⁹ M. Stepanov,⁴⁷ A. Ster,⁶⁸ S.P. Stoll,⁶ T. Sugitate,²³ C. Suire,⁵⁰ A. Sukhanov,⁶ J. Sun,⁶⁰ J. Sziklai,⁶⁸ E.M. Takagui,⁵⁷ A. Takahara,¹¹ A. Taketani,^{53,54} R. Tanabe,⁶⁴ Y. Tanaka,⁴⁵ S. Taneja,⁶⁰ K. Tanida,^{34,53,54,58} M.J. Tannenbaum,⁶ S. Tarafdar,³ A. Taranenko,⁵⁹ P. Tarján,¹⁶ E. Tennant,⁴⁷ H. Themann,⁶⁰ D. Thomas,¹ T.L. Thomas,⁴⁶ M. Togawa,^{34,53,54} A. Toia,⁶⁰ L. Tomášek,²⁷ M. Tomášek,²⁷ Y. Tomita,⁶⁴ H. Torii,^{23,53} R.S. Towell,¹ V-N. Tram,³⁵ I. Tserruya,⁶⁷ Y. Tsuchimoto,²³ K. Utsunomiya,¹¹ C. Vale,^{6,28} H. Valle,⁶⁵ H.W. van Hecke,³⁷ E. Vazquez-Zambrano,¹³ A. Veicht,^{13,25} J. Velkovska,⁶⁵ R. Vértési,^{16,68} A.A. Vinogradov,³³ M. Virius,¹⁴ A. Vossen,²⁵ V. Vrba,²⁷ E. Vznuzdaev,⁵² X.R. Wang,⁴⁷ D. Watanabe,²³ K. Watanabe,⁶⁴ Y. Watanabe,^{53,54} Y.S. Watanabe,¹¹ F. Wei,²⁸ R. Wei,⁵⁹ J. Wessels,⁴² S.N. White,⁶ D. Winter,¹³ C.L. Woody,⁶ R.M. Wright,¹ M. Wysocki,¹² W. Xie,⁵⁴ Y.L. Yamaguchi,^{11,66} K. Yamaura,²³ R. Yang,²⁵ A. Yanovich,²⁴ J. Ying,²¹ S. Yokkaichi,^{53,54} J.S. Yoo,¹⁸ Z. You,^{37,51} G.R. Young,⁴⁹ I. Younus,⁴⁶ I.E. Yushmanov,³³ W.A. Zajc,¹³ O. Zaudtke,⁴² A. Zelenski,⁵ C. Zhang,⁴⁹ S. Zhou,¹⁰ and L. Zolin²⁹

(PHENIX Collaboration)

¹Abilene Christian University, Abilene, Texas 79699, USA

²Institute of Physics, Academia Sinica, Taipei 11529, Taiwan

³Department of Physics, Banaras Hindu University, Varanasi 221005, India

⁴Bhabha Atomic Research Centre, Bombay 400 085, India

⁵Collider-Accelerator Department, Brookhaven National Laboratory, Upton, New York 11973-5000, USA

⁶Physics Department, Brookhaven National Laboratory, Upton, New York 11973-5000, USA

⁷University of California - Riverside, Riverside, California 92521, USA

⁸Charles University, Ovocný trh 5, Praha 1, 116 36, Prague, Czech Republic

⁹Chonbuk National University, Jeonju, 561-756, Korea

¹⁰Science and Technology on Nuclear Data Laboratory, China Institute of Atomic Energy, Beijing 102413, P. R. China

¹¹Center for Nuclear Study, Graduate School of Science, University of Tokyo, 7-3-1 Hongo, Bunkyo, Tokyo 113-0033, Japan

¹²University of Colorado, Boulder, Colorado 80309, USA

¹³Columbia University, New York, New York 10027 and Nevis Laboratories, Irvington, New York 10533, USA

¹⁴Czech Technical University, Zikova 4, 166 36 Prague 6, Czech Republic

¹⁵Dapnia, CEA Saclay, F-91191, Gif-sur-Yvette, France

¹⁶Debrecen University, H-4010 Debrecen, Egyetem tér 1, Hungary

¹⁷ELTE, Eötvös Loránd University, H - 1117 Budapest, Pázmány P. s. 1/A, Hungary

¹⁸Ewha Womans University, Seoul 120-750, Korea

¹⁹Florida Institute of Technology, Melbourne, Florida 32901, USA

²⁰Florida State University, Tallahassee, Florida 32306, USA

²¹Georgia State University, Atlanta, Georgia 30303, USA

²²Hanyang University, Seoul 133-792, Korea

²³Hiroshima University, Kagamiyama, Higashi-Hiroshima 739-8526, Japan

²⁴IHEP Protvino, State Research Center of Russian Federation, Institute for High Energy Physics, Protvino, 142281, Russia

²⁵University of Illinois at Urbana-Champaign, Urbana, Illinois 61801, USA

²⁶Institute for Nuclear Research of the Russian Academy of Sciences, prospekt 60-letiya Oktyabrya 7a, Moscow 117312, Russia

²⁷Institute of Physics, Academy of Sciences of the Czech Republic, Na Slovance 2, 182 21 Prague 8, Czech Republic

²⁸Iowa State University, Ames, Iowa 50011, USA

²⁹Joint Institute for Nuclear Research, 141980 Dubna, Moscow Region, Russia

³⁰Helsinki Institute of Physics and University of Jyväskylä, P.O.Box 35, FI-40014 Jyväskylä, Finland

³¹KEK, High Energy Accelerator Research Organization, Tsukuba, Ibaraki 305-0801, Japan

³²Korea University, Seoul, 136-701, Korea

³³Russian Research Center "Kurchatov Institute", Moscow, 123098 Russia

³⁴Kyoto University, Kyoto 606-8502, Japan

³⁵Laboratoire Leprince-Ringuet, Ecole Polytechnique, CNRS-IN2P3, Route de Saclay, F-91128, Palaiseau, France

³⁶Lawrence Livermore National Laboratory, Livermore, California 94550, USA

³⁷Los Alamos National Laboratory, Los Alamos, New Mexico 87545, USA

³⁸LPC, Université Blaise Pascal, CNRS-IN2P3, Clermont-Fd, 63177 Aubiere Cedex, France

³⁹Department of Physics, Lund University, Box 118, SE-221 00 Lund, Sweden

⁴⁰University of Maryland, College Park, Maryland 20742, USA

⁴¹Department of Physics, University of Massachusetts, Amherst, Massachusetts 01003-9337, USA

⁴²Institut für Kernphysik, University of Muenster, D-48149 Muenster, Germany

⁴³Muhlenberg College, Allentown, Pennsylvania 18104-5586, USA

- ⁴⁴Myongji University, Yongin, Kyonggido 449-728, Korea
⁴⁵Nagasaki Institute of Applied Science, Nagasaki-shi, Nagasaki 851-0193, Japan
⁴⁶University of New Mexico, Albuquerque, New Mexico 87131, USA
⁴⁷New Mexico State University, Las Cruces, New Mexico 88003, USA
⁴⁸Department of Physics and Astronomy, Ohio University, Athens, Ohio 45701, USA
⁴⁹Oak Ridge National Laboratory, Oak Ridge, Tennessee 37831, USA
⁵⁰IPN-Orsay, Universite Paris Sud, CNRS-IN2P3, BP1, F-91406, Orsay, France
⁵¹Peking University, Beijing 100871, P. R. China
⁵²PNPI, Petersburg Nuclear Physics Institute, Gatchina, Leningrad region, 188300, Russia
⁵³RIKEN Nishina Center for Accelerator-Based Science, Wako, Saitama 351-0198, Japan
⁵⁴RIKEN BNL Research Center, Brookhaven National Laboratory, Upton, New York 11973-5000, USA
⁵⁵Physics Department, Rikkyo University, 3-34-1 Nishi-Ikebukuro, Toshima, Tokyo 171-8501, Japan
⁵⁶Saint Petersburg State Polytechnic University, St. Petersburg, 195251 Russia
⁵⁷Universidade de São Paulo, Instituto de Física, Caixa Postal 66318, São Paulo CEP05315-970, Brazil
⁵⁸Seoul National University, Seoul, Korea
⁵⁹Chemistry Department, Stony Brook University, SUNY, Stony Brook, New York 11794-3400, USA
⁶⁰Department of Physics and Astronomy, Stony Brook University, SUNY, Stony Brook, New York 11794-3400, USA
⁶¹SUBATECH (Ecole des Mines de Nantes, CNRS-IN2P3, Université de Nantes) BP 20722 - 44307, Nantes, France
⁶²University of Tennessee, Knoxville, Tennessee 37996, USA
⁶³Department of Physics, Tokyo Institute of Technology, Oh-okayama, Meguro, Tokyo 152-8551, Japan
⁶⁴Institute of Physics, University of Tsukuba, Tsukuba, Ibaraki 305, Japan
⁶⁵Vanderbilt University, Nashville, Tennessee 37235, USA
⁶⁶Waseda University, Advanced Research Institute for Science and Engineering, 17 Kikui-cho, Shinjuku-ku, Tokyo 162-0044, Japan
⁶⁷Weizmann Institute, Rehovot 76100, Israel
⁶⁸Institute for Particle and Nuclear Physics, Wigner Research Centre for Physics, Hungarian Academy of Sciences (Wigner RCP, RMKI) H-1525 Budapest 114, POBox 49, Budapest, Hungary
⁶⁹Yonsei University, IPAP, Seoul 120-749, Korea
- (Dated: September 12, 2018)

The three Υ states, $\Upsilon(1S+2S+3S)$, are measured in d +Au and p + p collisions at $\sqrt{s_{NN}}=200$ GeV and rapidities $1.2 < |y| < 2.2$ by the PHENIX experiment at the Relativistic Heavy-Ion Collider. Cross sections for the inclusive $\Upsilon(1S+2S+3S)$ production are obtained. The inclusive yields per binary collision for d +Au collisions relative to those in p + p collisions (R_{dAu}) are found to be 0.62 ± 0.26 (stat) ± 0.13 (syst) in the gold-going direction and 0.91 ± 0.33 (stat) ± 0.16 (syst) in the deuteron-going direction. The measured results are compared to a nuclear-shadowing model, EPS09 [JHEP **04**, 065 (2009)], combined with a final-state breakup cross section, σ_{br} , and compared to lower energy p +A results. We also compare the results to the PHENIX J/ψ results [Phys. Rev. Lett. **107**, 142301 (2011)]. The rapidity dependence of the observed Υ suppression is consistent with lower energy p +A measurements.

PACS numbers: 25.75.Dw

I. INTRODUCTION

Quarkonia are produced dominantly by the gluon-gluon fusion process in high energy collisions [1, 2]. Therefore, quarkonia production is a good probe to explore the gluon distribution of the nucleon and its modification in nuclei. Recently, the PHENIX collaboration has reported J/ψ suppression in $\sqrt{s_{NN}}=200$ GeV deuteron-gold (d +Au) collisions at the Relativistic Heavy Ion Collider [3]. The centrality dependence of these J/ψ suppression results at forward rapidity is not well described quantitatively by nuclear-shadowing models that include final-state breakup effects [4]. Because the Υ mass is heavier than J/ψ , the nuclear effects on the gluon distri-

bution can be studied in different kinematic regions. At forward rapidity (the deuteron going direction) and the same collision energy of $\sqrt{s_{NN}}=200$ GeV, the average momentum fraction of the gluon in the gold nucleus that is sampled for Υ production is $\langle x_2 \rangle \approx 1 \times 10^{-2}$, whereas J/ψ production samples $\langle x_2 \rangle \approx 3 \times 10^{-3}$.

There are various fits for the nuclear parton distribution functions (nPDFs) over broad x ranges [5–9]. In d +Au collisions, since the forward and backward rapidities cover different x_2 (x in the Au nucleus) ranges, Υ production at these two rapidities would be affected differently by these nPDFs. Additionally, the final-state breakup effect should also suppress Υ yields by some amount at both rapidities, but there is no clear indication of the size of this effect yet [10]. Thus, Υ measurements in d +Au collisions should give new and valuable information to test nuclear parton modification and breakup effects.

Lattice quantum chromodynamics predicts that the

*Deceased

†PHENIX Spokesperson: jacak@skipper.physics.sunysb.edu

$\Upsilon(1S)$, $\Upsilon(2S)$, and $\Upsilon(3S)$ all have different binding energies and radii, and so should melt at different temperatures of the hot nuclear medium [11]. Therefore, the three Υ states are thought to be good probes for the temperature of the hot dense matter. Recently, the Compact Muon Solenoid (CMS) experiment at the Large Hadron Collider (LHC) reported that the double ratio of the $\Upsilon(2S+3S)$ excited states to the $\Upsilon(1S)$ ground state in Pb+Pb and $p+p$ collisions at $\sqrt{s_{NN}}=2.76$ TeV,

$$\frac{\Upsilon(2S+3S)/\Upsilon(1S)|_{\text{Pb+Pb}}}{\Upsilon(2S+3S)/\Upsilon(1S)|_{p+p}} = 0.31^{+0.19}_{-0.15}(\text{stat}) \pm 0.03(\text{syst})$$

for single decay muons of $p_T > 4$ GeV/ c and $|\eta| < 2.4$ [12]. They also reported $\Upsilon(1S)$ is suppressed by approximately 40% in minimum-bias Pb+Pb collisions [12].

In Υ suppression for nucleus-nucleus collisions, there should be contributions from cold nuclear matter as well as those from the hot nuclear matter. Thus, to separate these two types of contributions, it is necessary to measure the level of suppression from cold nuclear matter effects with $p(d)+A$ collisions, where hot nuclear matter is not created.

A lower-energy fixed-target experiment, E772, reported measurements in $\sqrt{s_{NN}}=38.8$ GeV $p+A$ collisions of the $\Upsilon(1S)$ ground state and the $\Upsilon(2S+3S)$ excited states. The observed suppression of the $\Upsilon(1S)$ and $\Upsilon(2S+3S)$ agree within the experimental uncertainties [13]. The initial-state effects from nuclear shadowing are not expected to differ between the three Υ states since they are produced mostly by gluon-gluon fusion subprocesses and have similar masses [1, 2, 10]. For the final-state breakup effect, there is no clear estimate of its energy dependence and of the difference between the three Υ states. In this paper, we present the first measurement of inclusive $\Upsilon(1S+2S+3S)$ cold nuclear matter effects as well as the production cross section using $d+Au$ and $p+p$ collisions at $\sqrt{s_{NN}}=200$ GeV measured by the PHENIX experiment.

II. ANALYSIS METHOD

A. Experimental setup

The PHENIX apparatus is described in detail in Ref. [14]. In $d+Au$ collisions, the deuteron comes from the negative-rapidity end of PHENIX (South) and goes towards positive-rapidity (North), and vice versa for the gold ions. For the Υ analysis presented here, three detector systems are required for reconstruction and triggering at forward and backward rapidities. These are the Muon Tracker (MuTr), the Muon Identifier (MuID), and the beam-beam counters (BBCs). There are two separate BBC systems. One covers forward rapidity and the other covers backward rapidity as shown in Fig. 1.

Each BBC comprises 64 quartz Čerenkov radiators and mesh dynode PMTs. The two BBCs are located at

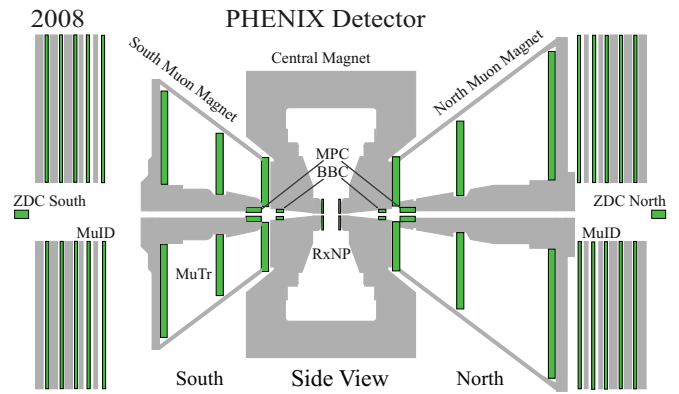


FIG. 1: (color online) PHENIX detector configuration in 2008. This side view includes the forward-rapidity detectors (South and North arms): the Muon Tracker (MuTr), the Muon Identifier (MuID) for muon detection and identification, and the beam-beam counter (BBC) for global event characteristics.

± 144 cm from the nominal interaction point and cover pseudorapidity of $3 < |\eta| < 3.9$. Each MuID comprises five layers of thick steel vertical plates with Iarocci tubes between each pair of plates. Most hadrons are absorbed in the steel plates. Muons with more than 2.7 GeV/ c of momentum will pass through all layers of the MuID and reach the last gap. Each MuTr is composed of three stations of cathode strip chambers and measures the momentum and charge sign of the muon according to their bending in the magnetic field, with coverage in rapidity of $1.2 < |y| < 2.2$ for the Υ and full azimuthal coverage of $\phi \in [-\pi, \pi]$. The nose-cone absorber and the central-magnet pole face, which both lie between the interaction region and the innermost part of the muon tracker, also help to reduce hadron backgrounds, especially by eliminating many light hadrons (e.g. π , K) before they decay into secondary muons. Fewer than 1% of hadrons punch through the absorbers, reach the last gap of MuID, and become fake muon tracks.

The data sets used in this analysis were collected during 2006, 2008, and 2009 using the BBC Level-1 trigger. This BBC trigger requires hits in the negative and positive rapidity ends of the BBC in order to register an interaction and provide a minimum-bias trigger. The BBC also measures the z-vertex position of the interaction using time differences between its hits in the negative and positive rapidity directions. For this analysis, the z-vertex is required to be within ± 30 cm of the center of PHENIX, $z = 0$. Additionally, the MuID Level-1 trigger is used in order to require that at least two particles penetrate through the MuID to its last layer.

After removing bad runs, such as those with numerous high-voltage trips and significant detector performance variations, the integrated luminosities of the collected data are 69 nb^{-1} and 67 nb^{-1} for the positive and negative rapidity muon detectors in $d+Au$ collisions from 2008. Here, 69 nb^{-1} and 67 nb^{-1} correspond to 27.2 pb^{-1}

and 26.4 pb^{-1} when scaled by the number of participants. For the $p+p$ collisions, the integrated luminosities are 22.5 pb^{-1} and 22.2 pb^{-1} for the positive and negative rapidities from 2006 and 2009.

We apply quality-assurance cuts on the data to select good tracks and improve the signal-to-background ratio. We calculate the track χ^2 and vertex χ_{vtx}^2 , and match the tracks in the MuID and the MuTr at the first layer of the MuID in both position and angle. We also check the number of hits in a MuID road, which is a straight line that connects sets of hits in different layers of the MuID. We compare momenta of the two muons and remove pairs with a large asymmetry ($|(p_1 - p_2)/(p_1 + p_2)| > 0.6$) between the two momenta. These asymmetric-momenta pairs are largely from random pairs where one hadron has decayed into a muon inside the tracking volume and has been misreconstructed as a higher momentum track; thus yielding a fake high-mass pair. The efficiency loss from this cut for Υ s is less than 2%. The values of the cuts are determined using the PHENIX GEANT3-based [15] (PISA) detector simulations.

For this analysis, we form an invariant-mass distribution from the unlike-charge-sign (foreground) pairs of muon tracks. In addition to the quarkonia resonances including the Υ signal, the mass distribution also contains uncorrelated (combinatorial) background and correlated background pairs. There are two methods to estimate the combinatorial backgrounds: 1) use like-sign pairs of muons from the same event, or 2) use an event-mixing method which mixes unlike-sign muons from different events to form random pairs. In this analysis, we use the event-mixing method to estimate the combinatorial background as shown in Fig. 2 (a), (c) and (e), and assign a systematic uncertainty based on the difference between the two methods. We calculate the normalization factor for the mixed events by

$$\text{Normalization Factor} = \frac{2 \times \sqrt{FG_{++} \times FG_{--}}}{BG_{+-}}. \quad (1)$$

Here, BG_{+-} stands for the number of the unlike-sign mixed events, FG_{++} and FG_{--} represent the number of the like-sign events. Unlike-sign mixed events are scaled by the normalization factor and we assign a 3% systematic uncertainty for this factor.

After the combinatorial background is subtracted, in the Υ -mass region, there are still contributions from correlated backgrounds expected from the Drell-Yan process and pairs of muons from the same $c\bar{c}$ or $b\bar{b}$ pairs. Therefore, it is important to estimate the correlated backgrounds properly to extract the Υ signal. We use next-to-leading order (NLO) calculations and PYTHIA 6.4 [16] to estimate these correlated backgrounds, and the PHENIX GEANT3 simulation to include a realistic detector response as shown in Fig. 2 (b), (d) and (f). Details of the estimates for these correlated backgrounds are described in the following sections.

B. Υ and physical background estimation

1. The Drell-Yan process

The mass region between 4 and 8 GeV/c^2 (above the J/ψ , ψ' masses and below the Υ mass) is dominated by the Drell-Yan process and by correlated open-heavy flavor pairs. The very low statistics above the Υ mass, where the Drell-Yan process dominates, does not provide a useful constraint on the Drell-Yan yield; so, we use NLO calculations from Vitev [17] to constrain the Drell-Yan yields and to estimate their contribution in the Υ -mass region. NLO calculations of the Drell-Yan process are known to be very accurate from comparisons to data at other energies [17, 19, 20]. For $d+\text{Au}$ collisions, nuclear effects are added in the NLO calculations - including isospin effects which account for the composition of the nucleus in terms of neutrons and protons, parton shadowing corrections, and the effect of initial-state energy loss [17].

To evaluate the model's systematic uncertainty for the Drell-Yan contribution, we use a calculation from CTEQ [18], as shown in Fig. 3a. For the Vitev calculation [17] without nuclear corrections, the difference between the CTEQ calculation and that from Vitev is approximately 10% over the entire mass range (filled-green squares and the black circles in Fig. 3b). We assume this same systematic uncertainty for $p+p$ and $d+\text{Au}$ collisions. Additionally, the variation of the renormalization and factorization scales in the calculation from Vitev, $Q/2 \leq \mu \leq 2Q$, is included as a systematic uncertainty for both collision systems.

The Drell-Yan contribution to the data is determined using the calculated cross section and the integrated luminosity for each data set. This contribution is corrected for geometrical acceptance and efficiencies. Details are shown in Eq. (2, 3, and (4); and are discussed in the text that follows.

$$\frac{d\sigma_{\text{DY}}}{dm} \cdot \mathcal{L} \cdot \epsilon_{\text{DY}}^{\text{BBC}} \cdot A\epsilon_{\text{DY}} = \frac{N_{\text{DY}}}{\Delta m}, \quad (2)$$

$$\frac{d\sigma_{\text{DY}}}{dm} \cdot \frac{N_{\text{MB}}}{\sigma_{\text{Tot}} \cdot \epsilon_{\text{MB}}^{\text{BBC}}} \cdot \epsilon_{\text{DY}}^{\text{BBC}} \cdot A\epsilon_{\text{DY}} = \frac{N_{\text{DY}}}{\Delta m}, \quad (3)$$

$$\frac{d\sigma_{\text{DY}}}{dm} \cdot \frac{N_{\text{MB}}}{\sigma_{\text{Tot}} \cdot C} \cdot A\epsilon_{\text{DY}} = \frac{N_{\text{DY}}}{\Delta m}, \quad (4)$$

where $d\sigma_{\text{DY}}/dm$ is the differential cross section of the Drell-Yan process, $q\bar{q} \rightarrow \gamma^* \rightarrow \mu^+\mu^-$, from the NLO calculation for each mass bin in the rapidity region $1.2 < |y| < 2.2$. \mathcal{L} stands for the integrated luminosity, $N_{\text{MB}}/(\sigma_{\text{Tot}} \cdot \epsilon_{\text{MB}}^{\text{BBC}})$, where N_{MB} stands for the number of sampled minimum-bias (MB) events and σ_{Tot} represents the total inelastic BBC MB cross section, 42.2 mb (2260 mb) for $p+p$ ($d+\text{Au}$) collisions. $\epsilon_{\text{MB}}^{\text{BBC}}$ and $\epsilon_{\text{DY}}^{\text{BBC}}$

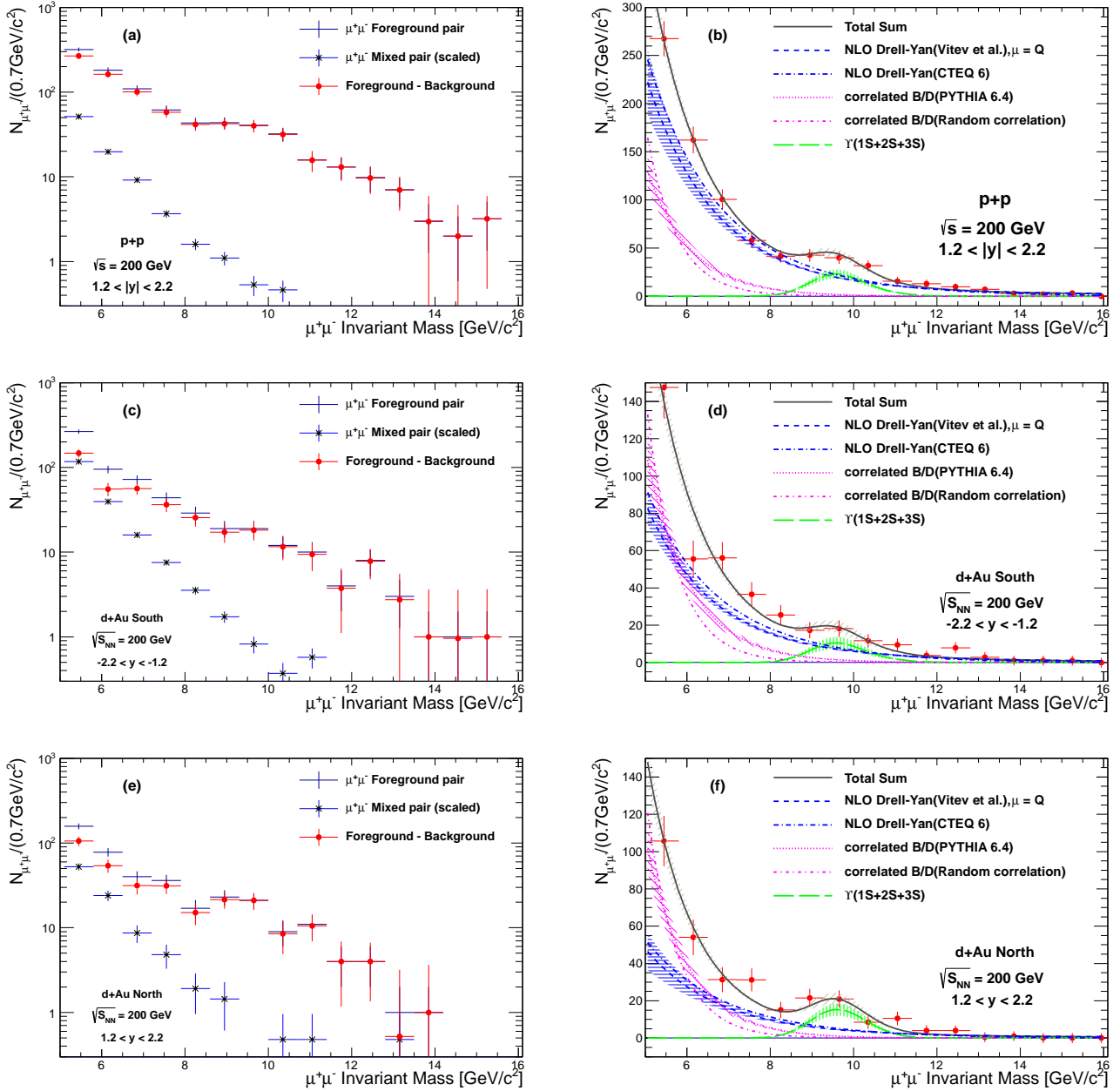


FIG. 2: (color online) The invariant mass distributions between $5 \text{ GeV}/c^2$ and $16 \text{ GeV}/c^2$ are shown for $p+p$ collisions (a,b) and in $d+Au$ collisions for the South arm (c,d) and the North arm (e,f). In the mass distributions, (a), (c), and (e) show the mass distribution of unlike-sign foreground pairs, the mixed event pairs as combinatorial background, and the subtraction of background pairs from foreground pairs. (b), (d), and (f) show the combinatorial background subtracted signal overlaid with the correlated backgrounds and $\Upsilon(1S+2S+3S)$. The shaded bands around the curves represent the uncertainties from the fitting or calculations of the renormalization and factorization scales, $Q/2 \leq \mu \leq 2Q$.

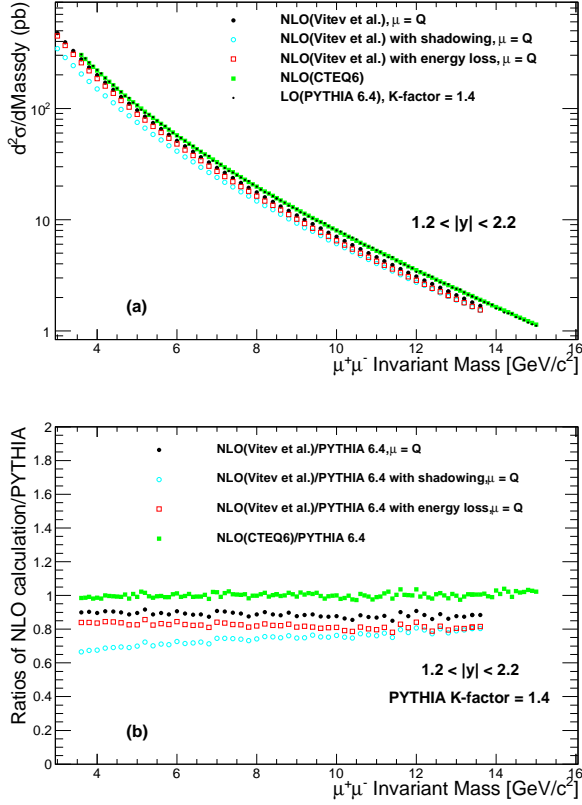


FIG. 3: (color online) Differential cross sections for the Drell-Yan process, $q\bar{q} \rightarrow \gamma^* \rightarrow \mu^+\mu^-$ are drawn (a) for a PYTHIA calculation and for NLO calculations [17, 18] in the rapidity region $1.2 < |y| < 2.2$. The ratios of the NLO calculations over that from PYTHIA 6.4 (K -factor=1.4) are also shown (b).

are the BBC trigger efficiencies for MB events and Drell-Yan events, respectively. $C = \epsilon_{\text{MB}}^{\text{BBC}} / \epsilon_{\text{DY}}^{\text{BBC}}$ is a correction factor for the relative BBC efficiencies of minimum bias compared to hard processes containing a Drell-Yan pair. Its value is determined using a Glauber model and a simulation of the BBC, and is 0.69 (0.89) for $p+p$ ($d+Au$) collisions. $A\epsilon_{\text{DY}}$ represents the product of the detector acceptance and efficiency, including the effect of the Level-1 trigger. Finally, $N_{\text{DY}}/\Delta m$ is the yield of dimuon pairs from the Drell-Yan process for each mass bin.

The detailed procedure to estimate the Drell-Yan yields for $p+p$ and $d+Au$, using Eq. (2) is as follows. First, we generate the correct number of Drell-Yan events, which we estimate by multiplying the differential cross section by the accumulated luminosity for each invariant mass bin considering BBC efficiencies. This corresponds to $d\sigma_{\text{DY}}/dm \cdot \mathcal{L} \cdot \epsilon_{\text{DY}}^{\text{BBC}}$ in Eq. (2). For example, \mathcal{L} is 22.5 pb^{-1} for the forward-rapidity $p+p$ data. After event generation, to account for the acceptance times efficiency, $A\epsilon_{\text{DY}}$, the generated Drell-Yan events from the luminosity-weighted NLO calculation are then run through the PHENIX GEANT3 simulation and are reconstructed in the same way as real data. In the simulation,

hit positions in all the muon detectors are registered and are reconstructed, including the effects of disabled HV channels and detector efficiencies. The resulting simulated counts in mass bins, $N_{\text{DY}}/\Delta m$, are then fit with an exponential function. This function describes the simulated distribution very well with a fit quality of χ^2 per degree-of-freedom (χ^2/dof) of 34.9/36 to 38.9/36. The shape and yield of this function are then fixed and used in the fits to the data, and represent the contribution of Drell-Yan in the fit function, Eq. (8).

Although the NLO cross sections for $d+Au$ collisions already include nuclear corrections, they are still per nucleon-nucleon collision, and need to be scaled up by the number of binary collisions, N_{coll} . Eq. (7) shows the relation between the cross section for $p+p$ and that for $d+Au$ collisions, which is derived from Eq. (5).

$$R_{dAu} = 1 = \frac{dN_{\text{DY}}^{dAu}/dm}{\langle N_{\text{coll}} \rangle dN_{\text{DY}}^{pp}/dm}, \quad (5)$$

$$\frac{\sigma_{\text{Tot}}^{dAu}}{\sigma_{\text{Tot}}^{pp}} = \frac{(dN_{\text{DY}}^{dAu}/dm) \cdot \sigma_{\text{Tot}}^{dAu}}{\langle N_{\text{coll}} \rangle (dN_{\text{DY}}^{pp}/dm) \cdot \sigma_{\text{Tot}}^{pp}} = \frac{d\sigma_{\text{DY}}^{dAu}/dm}{\langle N_{\text{coll}} \rangle d\sigma_{\text{DY}}^{pp}/dm}, \quad (6)$$

$$d\sigma_{\text{DY}}^{dAu}/dm = \langle N_{\text{coll}} \rangle d\sigma_{\text{DY}}^{pp}/dm \frac{\sigma_{\text{Tot}}^{dAu}}{\sigma_{\text{Tot}}^{pp}}, \quad (7)$$

where $dN_{\text{DY}}^{dAu(pp)}/dm$ is the invariant yield for the Drell-Yan process in $d+Au$ ($p+p$) collisions and $\sigma_{\text{Tot}}^{dAu(pp)}$ is the total inelastic cross section for $d+Au$ ($p+p$) collisions. In the expansion of Eq. (6), $dN_{\text{DY}}^{dAu(pp)}/dm \cdot \sigma_{\text{Tot}}^{dAu(pp)}$ is the differential cross section for the Drell-Yan process, $d\sigma_{\text{DY}}^{dAu(pp)}/dm$. $\langle N_{\text{coll}} \rangle$ is the mean number of binary collisions and is calculated using a Glauber model and a simulation of the BBC. $\langle N_{\text{coll}} \rangle$ is 7.6 ± 0.4 for inclusive $d+Au$ collisions. Eq. (7) is used for the Drell-Yan estimates in $d+Au$ collisions and $d\sigma_{\text{DY}}^{pp}/dm$ is considered as nuclear-effect-corrected cross sections per nucleon-nucleon before scaling up.

2. Correlations of open heavy-flavor pairs

Several measurements of open bottom and charm cross sections have been made by PHENIX. A recent single-electron measurement of heavy-quark production at midrapidity obtained $\sigma_{e\bar{e}} = 551 \pm 57$ (stat) ± 195 (syst) μb [23] for the total charm cross section. A dielectron measurement of the continuum charm pairs showed a total cross section of $\sigma_{e\bar{e}} = 544 \pm 39$ (stat) ± 142 (syst) ± 200 (model) μb [22]. A perturbative-quantum-chromodynamics fixed-order-next-to-leading-log calculation [24] predicts a cross section of $256_{-146}^{+400} \mu\text{b}$, which is within experimental and theoretical uncertainties with these measurements.

TABLE I: Simulation parameter settings for open beauty(charm) production. We used PYTHIA 6.4 with the CTEQ5L parton distribution functions [21]. The PYTHIA tunes are from a PHENIX dilepton mass spectra study [22]

| Name of parameter | Setting |
|---------------------------------|-----------------------|
| Bottom (Charm) Quark production | on |
| Bottom (Charm) Quark mass | 4.1 (1.25) GeV/ c^2 |
| k_T | 1.5 GeV/ c |
| K -factor | 3.4 |
| Q^2 | 4 GeV 2 |

Existing bottom cross section measurements from PHENIX also agree within their uncertainties. An electron-hadron charge correlation measurement showed a total bottom cross section of $\sigma_{b\bar{b}}=3.2^{+1.2}_{-1.1}$ (stat) $^{+1.4}_{-1.3}$ (syst) μb [25] and a continuum mass distribution study obtained $\sigma_{b\bar{b}}=3.9 \pm 2.5$ (stat) $^{+3}_{-2}$ (syst) μb [22]. Meanwhile the calculation [24] predicts $\sigma_{b\bar{b}}=1.87^{+0.99}_{-0.67}$ μb [24], consistent with the measurements.

To obtain an estimate of the mass shape and to generate simulated charm- and bottom-pair background events (see Table I for the simulation settings), we use the PYTHIA 6.4 tune, the same as that used for the PHENIX dilepton mass spectrum study [22]. The generated events are run through the PHENIX GEANT3 simulation to account for the detector acceptance at forward-rapidity and are reconstructed by using identical code to that used to reconstruct the data, with the detector efficiencies included. Before reconstructing the simulated events, they are embedded into real events in order to match and evaluate the effects of the multiplicity that exists for the data.

The resulting mass spectrum is fit by an exponential function with (χ^2/dof) of 10.0/12 to 11.8/12, which is then used to represent the open heavy-flavor component in the fits to the data, as in Eq. (8). The shape is fixed and the normalization, or yield, is allowed to vary in the fits to the data. The data fit-values obtained are within a half sigma in the experimental uncertainties of the previously measured charm and bottom cross sections [22] (see Section II C for further detail on the fits). For the shape of the fit function, we assign a systematic uncertainty by varying the slopes by $\pm 10\%$ from the nominal values obtained from the simulation.

The relative ratio of bottom and charm production is fixed according to the measured production cross sections obtained in the PHENIX dilepton mass spectrum study [22] with $\sigma_{c\bar{c}}=544 \pm 39$ (stat) ± 142 (syst) ± 200 (model) μb and $\sigma_{b\bar{b}}=3.9 \pm 2.5$ (stat) $^{+3}_{-2}$ (syst) μb . Since these have large measurement uncertainties, we assign a systematic uncertainty for the relative ratio of bottom and charm production cross sections by varying this ratio by $\pm 100\%$ from the nominal value; however, this does not result in a significant difference for the Υ yield because the charm contribution is negligible in the Υ -mass region.

Finally, a random angular correlation of the two open bottoms that form a pair is considered as an extreme case for the bottom correlation since NLO effects or interactions with other particles could alter the muon directions and destroy the angular correlation of the two heavy quarks. The p_T spectra of the single muons from open heavy-flavor decay are sampled and the azimuthal correlation angle ϕ of the decay muons is randomized for each muon and then pairs are formed, effectively destroying the angular correlation. The resulting difference between PYTHIA estimation and random correlation is assigned as an additional systematic uncertainty.

3. Υ estimation

Since the PHENIX muon-arm mass resolution is not good enough to resolve the three states of the Υ as shown in Fig. 4, we use results from two experiments at different collision energies and at different colliding systems to obtain an estimate of the relative ratio of the three Υ states, for the purpose of getting a distribution of line shape versus mass. The first is E605 [26], a $p + A$ fixed target experiment at $\sqrt{s_{NN}}=38.8$ GeV and the second is CDF [27], a collider experiment with $p + \bar{p}$ collisions at $\sqrt{s}=1.8$ TeV. These two experiments measured almost the same balance of the three Υ states although their energies and collision types are quite different (Table II).

TABLE II: Relative strength of the three Υ states at CDF [27] and from FNAL E605 [26].

| Υ states | Mass | Branching ratio | $p + \bar{p}$ [27] | $p + A$ [26] |
|-------------------|---------------|-----------------------------------|--------------------|--------------|
| | (GeV/ c^2) | $\Upsilon \rightarrow \mu^+\mu^-$ | 1.8 TeV | 38.8 GeV |
| $\Upsilon(1S)$ | 9.46 | 2.48% | 73% | 72% |
| $\Upsilon(2S)$ | 10.02 | 1.93% | 17% | 19% |
| $\Upsilon(3S)$ | 10.36 | 2.29% | 10% | 9% |

As the energy of the measurement reported here is between those of the other measurements, we assume here that the composition of the three Υ states follows the ratio from CDF and assign a systematic uncertainty by varying the relative strength of the $\Upsilon(1S)$ over 0.73 ± 0.10 , with the fractions for the $\Upsilon(2S)$ and $\Upsilon(3S)$ changing accordingly. This uncertainty also accounts for the possibility that the 2S and 3S states might be suppressed more strongly than the 1S in $d + \text{Au}$ minimum-bias collisions, since it allows for a 30% reduction in the 2S and a 50% reduction in the 3S.

Υ simulations are performed for the three Υ states in order to estimate the effective Υ mass resolution and peak position for the real detector as well as to determine the acceptance-times-efficiency correction. To obtain these estimates, we generate the three Υ states with PYTHIA 6.4 and then process the generated Υ events through the PHENIX GEANT3 simulation to make events with hits in the detectors. These simulated events are

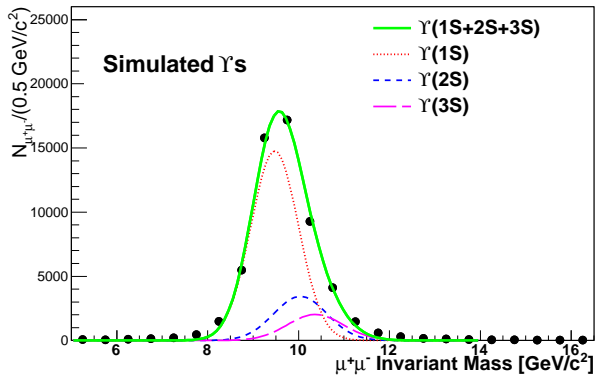


FIG. 4: (color online) $\Upsilon(1S+2S+3S)$ are generated using PYTHIA 6.4 and run through the PHENIX GEANT3 detector simulation. Each Υ has mass resolution of about $0.6 \text{ GeV}/c^2$. The line shape used for the fit function, Eq. (8) is composed of three Gaussians for the three Υ states.

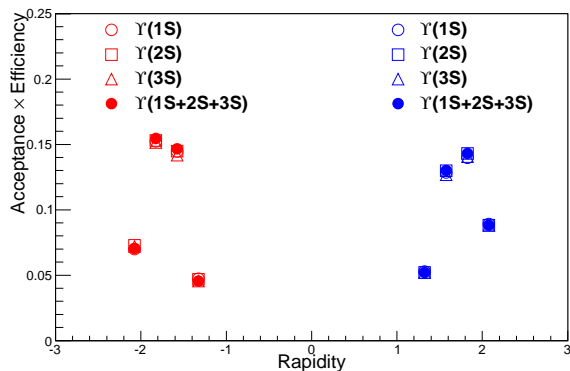


FIG. 5: (color online) Acceptance \times Efficiency of each Υ state and for the sum of the three states, $\Upsilon(1S+2S+3S)$. The values for each state and for the sum of the three states are very similar. The $\Upsilon(1S+2S+3S)$ is comprised of the $\Upsilon(1S)$, $\Upsilon(2S)$, and $\Upsilon(3S)$, following the abundances of 73% : 17% : 10% from the CDF experiment [27]. See also Table II.

then embedded into real events to reflect the multiplicity environment of the data and are reconstructed with iden-

tical code to that used to reconstruct the data - including resolution smearing effects. The sum of three Gaussian functions is fit to the Υ -mass distribution. The results from the fit provide an estimate of the widths and the means of masses for the three Υ states. The resulting shape, as shown in Fig. 4, is then implemented for the fit function, Eq. (8) used to extract the yields from the data.

Unlike the J/ψ , where the mass resolution is predominantly determined by effects from multiple scattering in the absorber preceding the muon-tracking volume, the higher momentum muons from the Υ experience less multiple scattering and less bending in the magnetic field; so the position resolution in the tracking volume becomes more important. To evaluate this, an additional systematic is obtained by allowing the mass resolutions of the three states to vary by $\pm 100 \text{ MeV}/c^2$ from their nominal, simulation determined, values.

With the simulated $\Upsilon(1S+2S+3S)$ events, we also calculate the acceptance times efficiency ($A\epsilon_\Upsilon$) by dividing the reconstructed Υ yields by the PYTHIA generated Υ yields. Figure 5 shows $A\epsilon_\Upsilon$ as a function of rapidity. $A\epsilon_\Upsilon$ of the summed $\Upsilon(1S+2S+3S)$ and of each Υ states separately are quite similar to each other as shown. In this analysis, two inclusive rapidity bins are used, one for the positive rapidity and one for the negative rapidity. The values in $d+\text{Au}$ collisions from 2008 are 0.0950 ± 0.0004 and 0.0980 ± 0.0004 for positive and negative rapidity, respectively. For $p+p$ collisions, in the rapidity same order, from 2006 they are 0.1132 ± 0.0007 and 0.1096 ± 0.0007 ; and from 2009, they are 0.1164 ± 0.0007 and 0.0907 ± 0.0007 .

C. Data evaluation and Υ extraction

We extract Υ s from the data using the estimated correlated backgrounds and the Υ s as described in Sections II B 1, II B 2, and II B 3. The fit function used for the mass distribution is shown in Eq. (8). In addition to the $\Upsilon(1S+2S+3S)$ signal, the function includes contributions from the Drell-Yan process and from correlated open bottom/charm pairs.

$$F(m) = p_0 \exp(p_1 m + p_2 m^2 + p_3 m^3) + p_4 [(1 - p_6) \exp(p_5 m) + p_6 \exp(p_7 m)] + p_8 [(1 - p_{11} - p_{14}) \exp(-0.5A^2) + p_{11} \exp(-0.5B^2) + p_{14} \exp(-0.5C^2)] \quad (8)$$

where m is the invariant mass of the dimuon, $A = (m - p_9)/p_{10}$, $B = (m - p_{12})/p_{13}$, and $C = (m - p_{15})/p_{16}$. The parameters p_0 to p_3 are for the NLO Drell-Yan process and are fixed by the NLO calculations and the PHENIX GEANT3 simulation, as discussed in Section II B 1.

The parameters p_4 to p_7 are for the contribution of the open bottom and open charm correlated pairs. The relative ratio of bottom to open charm yields, which is represented by p_6 , is fixed from the PHENIX dilepton mass spectra study [22], and the shape is determined from

TABLE III: Parameter settings for the fits to the data and extraction of the Υ s [Eq. (8)]. See text for the details.

| Parameter | Fitting Parameter | Setting |
|-----------|---|--|
| p_0 | Yield of Drell-Yan process | Fixed by NLO calculation |
| p_1 | Slope of Drell-Yan process | Fixed by NLO calculation |
| p_2 | Slope of Drell-Yan process | Fixed by NLO calculation |
| p_3 | Slope of Drell-Yan process | Fixed by NLO calculation |
| p_4 | Yield of Charm/Beauty correlations | Set free |
| p_5 | Slope of Beauty correlation | Fixed by PYTHIA/GEANT simulation |
| p_6 | Relative ratio of Charm/Beauty correlations | Fixed PHENIX dilepton measurement [22] |
| p_7 | Slope of Charm correlation | Fixed by PYTHIA/GEANT simulation |
| p_8 | Yield of $\Upsilon(1S+2S+3S)$ | Set free |
| p_9 | Mean value of $\Upsilon(1S)$ | Fixed by PYTHIA/GEANT simulation |
| p_{10} | Resolution of $\Upsilon(1S)$ | Fixed by PYTHIA/GEANT simulation |
| p_{11} | Relative ratio of $\Upsilon(2S)$ | Fixed by CDF experiment [27] |
| p_{12} | Mean value of $\Upsilon(2S)$ | Fixed by PYTHIA/GEANT simulation |
| p_{13} | Resolution of $\Upsilon(2S)$ | Fixed by PYTHIA/GEANT simulation |
| p_{14} | Relative ratio of $\Upsilon(3S)$ | Fixed by CDF experiment [27] |
| p_{15} | Mean value of $\Upsilon(3S)$ | Fixed by PYTHIA/GEANT simulation |
| p_{16} | Resolution of $\Upsilon(3S)$ | Fixed by PYTHIA/GEANT simulation |

TABLE IV: Systematic uncertainties for each source and for each collision type (see the text for details). Type A represents a point-to-point uncorrelated systematic uncertainty. Type B represents a common systematic uncertainty between points at different rapidity. Type C is a global uncertainty.

| Systematic uncertainty sources | $p+p$ South (backward rapidity) | $p+p$ North (forward rapidity) | $d+Au$ South (backward rapidity) | $d+Au$ North (forward rapidity) | Type |
|--|------------------------------------|-----------------------------------|-------------------------------------|------------------------------------|------|
| Relative ratio of $\Upsilon(1S+2S+3S)$ | 2.6 % | 0.8 % | 0.9 % | 2.6 % | A |
| Relative ratio of Bottom/Charm | 0.3 % | 0.1 % | 0.4 % | 0.3 % | A |
| Υ mass resolution | 6.4 % | 6.7 % | 7.9 % | 8.3 % | B |
| NLO DY model | 7.7 % | 6.9 % | 4.0 % | 4.4 % | B |
| NLO DY renormalization/factorization | 0.9 % | 0.9 % | 7.7 % | 2.2 % | B |
| Open Bottom random correlation | 7.2 % | 4.0 % | 9.2 % | 6.3 % | B |
| Combinatorial background normalization | 0.6 % | 0.7 % | 4.0 % | 2.3 % | B |
| Combinatorial background estimation methods of like-sign and mixed events | 1.7 % | 2.3 % | 0.0 % | 1.1 % | B |
| MuID efficiency | 4.0 % | 4.0 % | 4.0 % | 4.0 % | B |
| MuTr efficiency | 2.0 % | 2.0 % | 2.0 % | 2.0 % | B |
| BBC efficiency | 10.1 % | 10.1 % | 5.3 % | 5.3 % | C |

the PYTHIA and the PHENIX GEANT3 simulation, as described in Section II B 2. The total yield from correlated bottom and charm, p_4 , is allowed to vary in the fits to the data. The resulting contributions from correlated bottom and charm are then checked against those from the PHENIX dilepton measurements, which have bottom and charm cross sections of $\sigma_{c\bar{c}}=544 \pm 39$ (stat) ± 142 (syst) ± 200 (model) μb and $\sigma_{b\bar{b}}=3.9 \pm 2.5$ (stat) $^{+3}_{-2}$ (syst) μb [22]. For this check, we integrated our fitted correlated bottom and charm over the mass range 5

GeV/c^2 to 16 GeV/c^2 , and then added the contribution from unmeasured regions assuming the mass shape from the NLO calculation. This estimate of the contribution of bottom and charm is within a half sigma in the experimental uncertainties of the nominal cross sections. For $d+Au$ collisions, this estimate is still within a half sigma when we scale the nominal cross section by the number of participants (2×197) assuming no nuclear modification effects on the production.

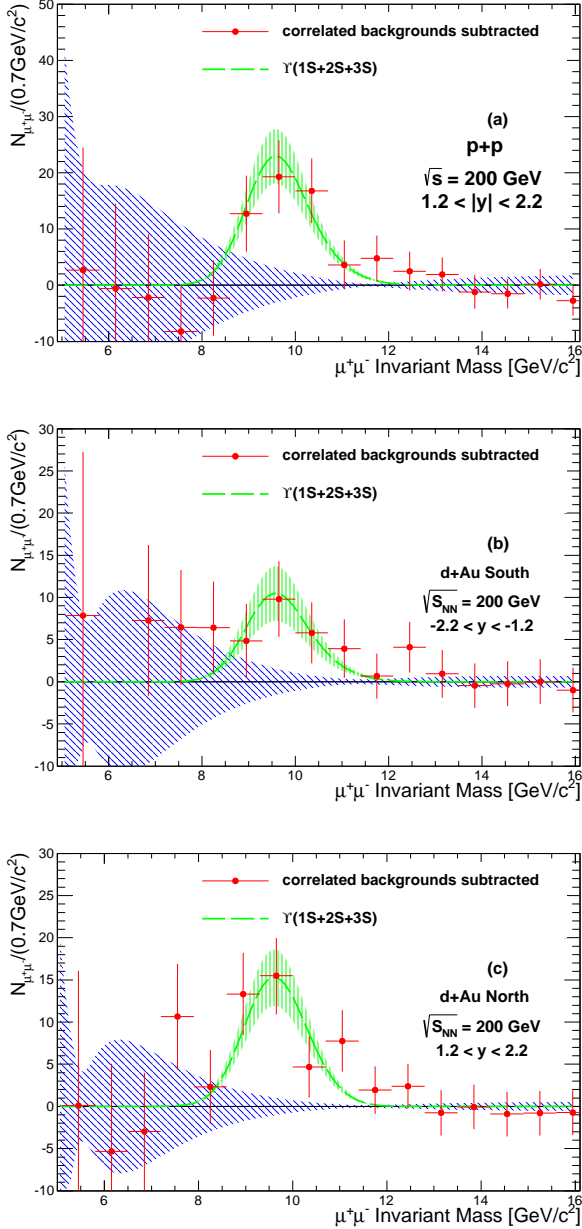


FIG. 6: (color online) The mass distributions are drawn after subtraction of all the correlated backgrounds and Drell-Yan process. The fitted peak curves represent only $\Upsilon(1S+2S+3S)$. The shaded bands (green vertical shading) around the fitted peak curves represent fitting uncertainties and those around zero yield (blue slanted shading) represent systematic uncertainties from the different assumptions for NLO Drell-Yan models, PYTHIA and random correlations of charm/bottom.

The parameters p_8 to p_{16} are for the contribution of the $\Upsilon(1S+2S+3S)$. A , B , and C represent the means of masses and widths of the three Υ states, as estimated using the PHENIX GEANT3 simulation package and fixed for data - as described in Section IIB 3. The total yield

of Υ , p_8 , is allowed to vary in the fits to the data in order to extract the Υ signal.

The data are fit using a log-likelihood fitting method that adds the normalized combinatorial background to both the mass distribution and the fit function. This has the advantage that empty bins in the mass distribution, which result from statistical fluctuations of the background above the signal size and otherwise produce negative counts, are accounted for properly. The fitting quality is very good with χ^2/dof of 9.0/16 and 6.4/16 for the negative and positive rapidities of $p+p$ collisions, respectively, and 14.6/16 and 9.5/16 for the negative and positive rapidities of $d+Au$ collisions, respectively. Systematic uncertainties from the NLO calculation, the assumed cross sections, and detector performances are explained in Sections IIB 1, IIB 2, and IIB 3, and are summarized in Table IV. Figure 6 (a), (b), and (c) show the $\Upsilon(1S+2S+3S)$ mass distribution after subtracting off all correlated backgrounds, for $p+p$ and $d+Au$ collision systems. We checked above the Υ -mass region, $> 11.5 \text{ GeV}/c^2$, for fitting reliability; the integral of the high-mass region is within the systematical uncertainties, which are drawn as shaded bands.

III. RESULTS AND DISCUSSION

TABLE V: Υ invariant yields and cross sections of $p+p$ and $d+Au$ data sets are shown. The first uncertainty shown is the statistical, and the second is the systematical.

| Data set | N_{MB}^{BBC} ($\times 10^{11}$) | $B_{\mu^+\mu^-} dN_{\Upsilon}/dy$ ($\times 10^{-10}$) | $B_{\mu^+\mu^-} d\sigma_{\Upsilon}/dy$ |
|--------------|--|--|--|
| $p+p$ South | 5.1 | $3.8 \pm 1.1 \pm 0.5$ | $16.0 \pm 4.6 \pm 2.2 \text{ pb}$ |
| $p+p$ North | 5.2 | $3.6 \pm 1.0 \pm 0.4$ | $15.4 \pm 4.3 \pm 1.8 \text{ pb}$ |
| $d+Au$ South | 1.3 | $17.8 \pm 5.5 \pm 2.9$ | $4.0 \pm 1.2 \pm 0.6 \text{ nb}$ |
| $d+Au$ North | 1.3 | $25.2 \pm 5.6 \pm 3.3$ | $5.7 \pm 1.3 \pm 0.7 \text{ nb}$ |

The invariant yields of $\Upsilon(1S+2S+3S)$ for each rapidity bin are calculated as,

$$B_{\mu^+\mu^-} \frac{dN_{\Upsilon}}{dy} = \frac{N_{\Upsilon} \cdot C}{N_{MB} \cdot A \epsilon_{\Upsilon} \cdot \Delta y}, \quad (9)$$

where the notation is the same as for Eq. (4), except Υ is used instead of the Drell-Yan process. Table V shows calculated yields and cross sections for both arms and for both collision types.

Figure 7 shows the invariant Υ yields for $p+p$ and $d+Au$ collisions. The nuclear modification factor, R_{dAu} , can be obtained from the invariant yields. Eq. (5) shows the relation between R_{dAu} , the invariant yield, and N_{coll} . The scale factor, N_{coll} , makes R_{dAu} one if the Υ yield for $d+Au$ collisions is equal to the Υ yield for $p+p$ collisions times the number of binary collisions in $d+Au$ collisions, i.e. $R_{dAu} = 1$ if there are no nuclear modification effects.

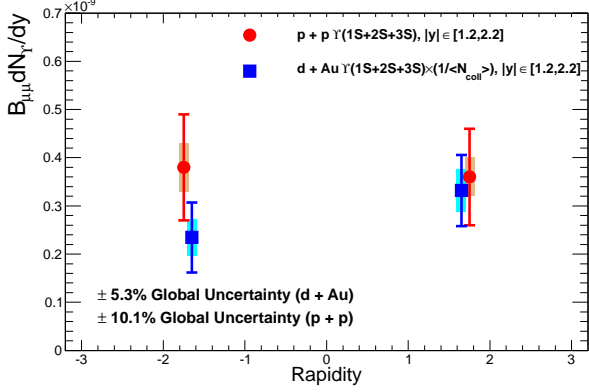


FIG. 7: (color online) Invariant yields, $B_{\mu\mu} dN_{\Upsilon}/dy$, for $p+p$ and $d+Au$ collisions are shown as a function of rapidity. The solid error bars represent the statistical uncertainties. The boxes represent the systematic uncertainties. The global systematic uncertainties are quoted as text at the bottom.

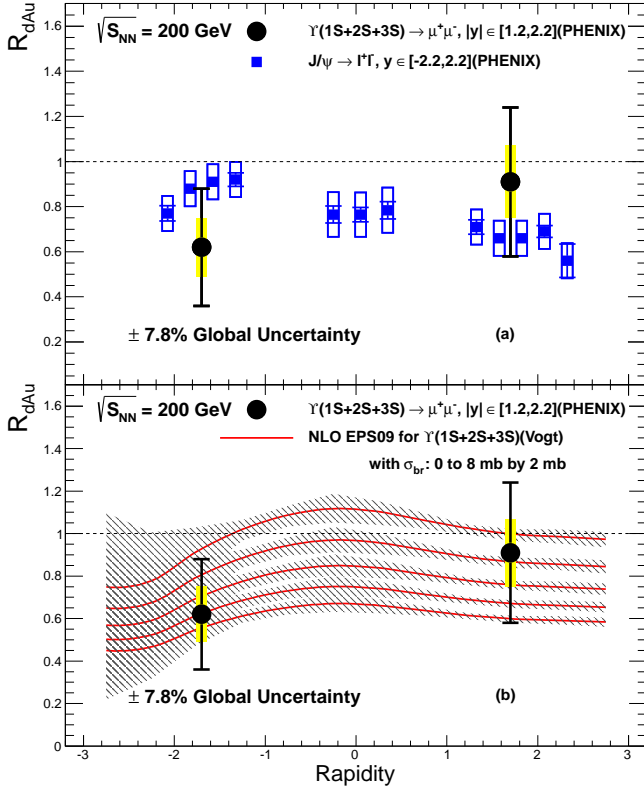


FIG. 8: (color online) Nuclear modification factors, R_{dAu} , are shown as a function of rapidity. For comparison, the upper panel (a) shows R_{dAu} for the J/ψ [3] as well as for the Υ . The solid error bars represent the statistical uncertainties and the boxes represent the systematic uncertainties. The global systematic uncertainty is quoted as text at the bottom. The lower panel (b) shows theoretical predictions of nuclear modification based on a NLO EPS09 combined with a breakup cross section, with $\sigma_{br}=0$ to 8 mb in 2 mb steps from top to bottom. See text for the details.

As seen in Fig. 8, at forward rapidity Υ production shows no significant suppression with an R_{dAu} of 0.91 ± 0.33 (stat) ± 0.16 (syst); while at backward rapidity the suppression of the Υ is approximately one sigma (of the experimental uncertainty) below one with an R_{dAu} of 0.62 ± 0.26 (stat) ± 0.13 (syst). Figure 8 (a) shows a comparison to previous results from PHENIX for R_{dAu} of the J/ψ . The J/ψ results show a larger suppression at forward than at backward rapidity, a trend that cannot be confirmed or denied for the Υ given the large uncertainties of the measurements presented here.

A NLO calculation with EPS09 shadowing and a breakup cross section [10] predicts modest suppression at backward rapidity, but no shadowing at forward rapidity; although there could be suppression by a breakup cross section, as seen in the red lines in Fig. 8 (b). The rapidity dependence of this NLO calculation appears to be consistent with the trend between our backward- and forward-rapidity measurements. At both backward and forward rapidities, the large uncertainties of the measurements do not give a significant constraint on the breakup cross section within the context of the NLO models. It will also be of interest to compare other models that include the effects of initial-state parton energy loss or of gluon saturation to this Υ data.

We can parameterize the nuclear dependence of Υ production as $\sigma_{\Upsilon}^{d+Au} = \sigma_{\Upsilon}^{p+p} \times (2A_{Au})^{\alpha}$ for $d+Au$ collisions, where A_{Au} represents the number of nucleons in the gold nucleus. As for R_{dAu} , if there are no nuclear effects then α would be one. Previously, E772, which was at $\sqrt{s_{NN}}=38.8$ GeV, showed a large decrease in α at $x_F < 0$. The PHENIX backward-rapidity covers $-0.42 \leq x_F \leq -0.14$, where $x_F = x_1 - x_2$ and x_1 is the momentum fraction of the gluon in deuteron. The backward-rapidity ($\langle x_F \rangle \sim -0.2$, $\langle x_2 \rangle \sim 2 \times 10^{-1}$) PHENIX measurements obtain $\alpha_{\Upsilon(1S+2S+3S)} = 0.925 \pm 0.070$ (stat) ± 0.035 (syst) and at forward rapidity ($\langle x_F \rangle \sim 0.2$, $\langle x_2 \rangle \sim 1 \times 10^{-2}$) $\alpha_{\Upsilon(1S+2S+3S)} = 0.990 \pm 0.060$ (stat) ± 0.029 (syst).

Figure 9 shows α versus x_F and versus x_2 from the E772 data and from our data. The suppression levels of $\Upsilon(1S+2S+3S)$ in PHENIX are consistent with those from E772 within uncertainties.

For our $d+Au$ measurements, we can also calculate the ratio of the Υ yield, dN_{Υ}^{d+Au}/dy , between backward and forward rapidities as a test of the nPDF. This ratio, $dN_{\Upsilon}^{d+Au}/dy|_{-2.2 < y < -1.2} / dN_{\Upsilon}^{d+Au}/dy|_{1.2 < y < 2.2}$, shows some suppression at backward rapidity relative to forward rapidity, with a value of 0.71 ± 0.27 (stat); but the effect is not very significant due to the large uncertainty.

IV. SUMMARY & CONCLUSION

In summary, we have presented the first yields, cross sections, and nuclear dependences for Υ production in

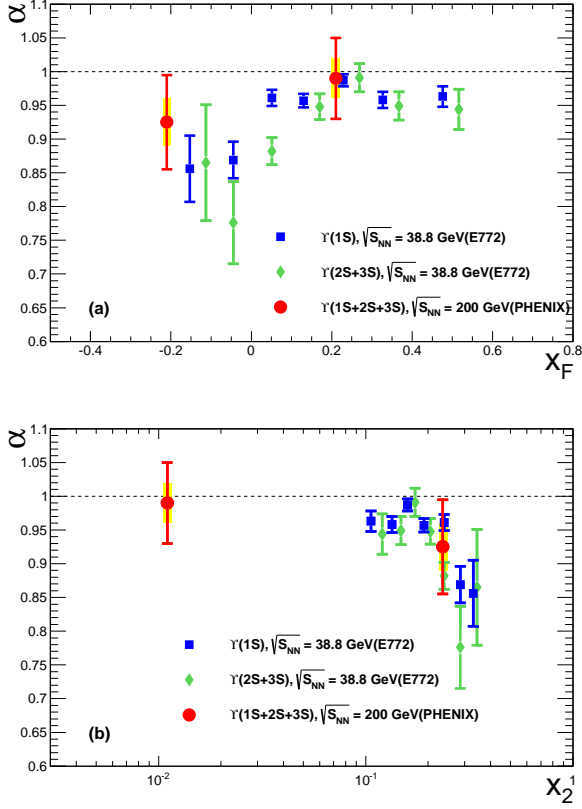


FIG. 9: (color online) α versus x_F and x_2 . The square and diamond shaped points are from the E772 experiment where an 800 GeV proton beam collides with fixed targets of ^2H , C, Ca, Fe and W, corresponding to $\sqrt{s_{NN}} = 38.8$ GeV. The round points are from this analysis. The solid error bars represent the statistical uncertainties and the boxes represent the systematic uncertainties.

$\sqrt{s_{NN}} = 200$ GeV $d+\text{Au}$ and $p+p$ collisions for two rapidity bins. At backward rapidity, $\Upsilon(1S+2S+3S)$ yields are measured to be suppressed by approximately one sigma of the experimental uncertainty below one. The rapidity dependence of the observed Υ suppression at forward and backward rapidities are compatible with lower energy results and a NLO theoretical calculation. Comparison to the theoretical calculation for a model that includes EPS09 shadowing and a breakup cross section does not result in any definitive constraint on the breakup

cross section given the large experimental uncertainties. Future comparisons to gluon saturation models and to models including initial-state energy loss would also be of interest.

Acknowledgements

We thank the staff of the Collider-Accelerator and Physics Departments at Brookhaven National Laboratory and the staff of the other PHENIX participating institutions for their vital contributions. We also thank Ramona Vogt, Ivan Vitev, and Rishi Sharma for useful discussions and theoretical calculations. We acknowledge support from the Office of Nuclear Physics in the Office of Science of the Department of Energy, the National Science Foundation, a sponsored research grant from Renaissance Technologies LLC, Abilene Christian University Research Council, Research Foundation of SUNY, and Dean of the College of Arts and Sciences, Vanderbilt University (U.S.A), Ministry of Education, Culture, Sports, Science, and Technology and the Japan Society for the Promotion of Science (Japan), Conselho Nacional de Desenvolvimento Científico e Tecnológico and Fundação de Amparo à Pesquisa do Estado de São Paulo (Brazil), Natural Science Foundation of China (P. R. China), Ministry of Education, Youth and Sports (Czech Republic), Centre National de la Recherche Scientifique, Commissariat à l'Énergie Atomique, and Institut National de Physique Nucléaire et de Physique des Particules (France), Bundesministerium für Bildung und Forschung, Deutscher Akademischer Austausch Dienst, and Alexander von Humboldt Stiftung (Germany), Hungarian National Science Fund, OTKA (Hungary), Department of Atomic Energy and Department of Science and Technology (India), Israel Science Foundation (Israel), National Research Foundation and WCU program of the Ministry Education Science and Technology (Korea), Ministry of Education and Science, Russian Academy of Sciences, Federal Agency of Atomic Energy (Russia), VR and Wallenberg Foundation (Sweden), the U.S. Civilian Research and Development Foundation for the Independent States of the Former Soviet Union, the Hungarian American Enterprise Scholarship Fund, and the US-Israel Binational Science Foundation.

[1] N. Brambilla et al., *Eur. Phys. J. C* **71**, 1534 (2011).
 [2] R. Vogt, *Phys. Rev. C* **61**, 035203 (2000).
 [3] A. Adare et al. (PHENIX Collaboration), *Phys. Rev. Lett.* **107**, 142301 (2011).
 [4] J. L. Nagle, A. D. Frawley, L. A. Linden Levy, and M. G. Wysocki, *Phys. Rev. C* **84**, 044911 (2011).
 [5] K. J. Eskola, H. Paukkunen, and C. A. Salgado, *JHEP* **04**, 065 (2009).

[6] K. J. Eskola, V. J. Kolhinen, and P. V. Ruuskanen, *Nucl. Phys. B* **535**, 351 (1998).
 [7] K. J. Eskola, V. J. Kolhinen, and C. A. Salgado, *Eur. Phys. J. C* **9**, 61 (1999).
 [8] K. J. Eskola, V. J. Kolhinen, and C. A. Paukkunen, H. and Salgado, *JHEP* **05**, 002 (2007).
 [9] D. de Florian and R. Sassot, *Phys. Rev. D* **69**, 074028 (2004).

- [10] R. Vogt, Phys. Rev. C **81**, 044903 (2010).
- [11] H. Satz, J. Phys. G **32**, R25 (2006).
- [12] S. Chatrchyan et al. (CMS Collaboration), Phys. Rev. Lett. **107**, 052302 (2011).
- [13] D. M. Alde et al., Phys. Rev. Lett. **66**, 2285 (1991).
- [14] K. Adcox et al. (PHENIX Collaboration), Nucl. Instrum. Methods A **499**, 469 (2003).
- [15] R. Brun, F. Bruyant, M. Maire, A. C. McPherson, and P. Zanarini (1987), cERN-DD-EE-84-1.
- [16] T. Sjostrand, S. Mrenna, and P. Skands, JHEP **05**, 026 (2006).
- [17] R. B. Neufeld, I. Vitev, and B.-W. Zhang, Phys. Lett. B **704**, 590 (2011).
- [18] J. Pumplin et al., JHEP **07**, 012 (2002).
- [19] J. C. Webb et al. (E866/NuSea Collaboration), arXiv:hep-ex/0302019 (2003).
- [20] T. Affolder et al. (CDF Collaboration), Phys. Rev. D **63**, 011101 (2000).
- [21] H. L. Lai et al. (CTEQ), Eur. Phys. J. C **12**, 375 (2000).
- [22] A. Adare et al. (PHENIX Collaboration), Phys. Lett. B **670**, 313 (2009).
- [23] A. Adare et al. (PHENIX Collaboration), Phys. Rev. C **84**, 044905 (2011).
- [24] M. Cacciari, P. Nason, and R. Vogt, Phys. Rev. Lett. **95**, 122001 (2005).
- [25] A. Adare et al. (PHENIX Collaboration), Phys. Rev. Lett. **103**, 082002 (2009).
- [26] G. Moreno et al., Phys. Rev. D **43**, 2815 (1991).
- [27] K. Ohl, Frascati Phys. Ser. **5**, 579 (1996).